Ice Crystal Concentrations in Wave Clouds: Dependencies on Temperature, D>0.5 μm Aerosol Particle Concentration and Duration of Cloud Processing

L.Peng, J.R. Snider and Z. Wang

Corresponding author: J.R. Snider
Department of Atmospheric Sciences
University of Wyoming, Laramie, WY

Abstract

Model equations used to either diagnose or prognose the concentration of heterogeneously nucleated ice crystals depend on combinations of cloud temperature, aerosol properties, and elapsed time of supersaturated-vapor or supercooled-liquid conditions. The validity of these equations is questioned. For example, there is concern that practical limitations on aerosol particle time-of-exposure to supercooled-liquid conditions, within ice nucleus counters, can bias model equations that have been constrained by ice nucleating particle (INP) measurements. In response to this concern, this work analyzes airborne measurements of crystals made within the downwind glaciated portions of wave clouds. A streamline model is used to connect a measurement of aerosol concentration, made upwind of a cloud, to a downwind ice crystal (IC) concentration. Four parameters were derived for 80 streamlines: (1) minimum cloud temperature along the streamline, (2) aerosol particle concentration (diameter, $D > 0.5$ μm) measured within ascending air, upwind of the cloud, (3) IC concentration measured in descending air downwind, and (4) the duration of water-saturated conditions along the streamline. The latter are between 38 to 507 s and the minimum temperatures are between −34 to −14 °C. Values of minimum temperature, $D > 0.5$ μm aerosol concentration and IC concentration were fitted using the equation developed for INPs by DeMott et al. (2010; D10). Overall, there is reasonable agreement among measured IC concentrations, INP concentrations derived using D10's fit equation, and IC concentrations derived by fitting the wave cloud measurements with the equation developed by D10.

1 - Introduction

Ice nucleation is a pivotal process in the evolution of many cloud types [Braham and Squires, 1974; Cantrell and Heymsfield, 2005; DeMott et al., 2010; Murray et al., 2012]. Ice crystals form via different pathways; the two fundamental distinctions are homogeneous and heterogeneous nucleation. Temperatures colder than -35 °C, and the existence of either haze particles or cloud droplets, are necessary conditions for the occurrence of the homogeneous pathway [Heymsfield and Miloshevich, 1993]. Heterogeneous ice nucleation takes place on ice nucleating particles (INPs) and the known pathways are deposition, condensation freezing, immersion freezing and contact freezing [Vali, 1985; Murray et al., 2012].

Two contrasting approaches are used to translate measurements into equations used to predict INP activation, and thus ice crystal (IC) concentration, in cloud models. The first of these is diagnostic in the sense that IC concentration is formulated solely in terms of thermodynamic and aerosol state properties. The second is state and time dependent. In model intercomparison studies [Eidhammer et al., 2009; Niemand et al., 2012], these two frameworks produce significantly different IC concentrations. There are many reasons for these inconsistencies; fundamentally, they result because the time scale characterizing the development of a subcritical ice embryo into an ice crystal [Bigg, 1953; Vali and Stansbury, 1966], and how properties of an ice nucleating particle influences embryo development, are inadequately understood [Murray et al., 2012; Vali, 2014]. Another relevant factor, but one which attenuates the framework-to-framework differences [Eidhammer et al., 2009], is that the Bergeron-Findeisen process can act to

55 slow, or even shut down, the freezing nucleation pathways (i.e., condensation, immersion
56 and contact freezing).

57 Our primary focus is the temperature- and aerosol-dependent fit equation
58 developed by DeMott et al. (2010; hereafter D10). The D10 equation, hereafter Eqn. 1,
59 was developed with measurements of activated INP concentration derived using the
60 continuous flow diffusion chamber (CFDC; Rogers et al., 2001). The INP measurements
61 were made concurrently with measurements of the concentration of aerosol particles with
62 diameter (D) larger than 0.5 µm ($n_{0.5}$)

63 $$N_{INP}(T, n_{0.5}) = a \cdot (T_o - T)^b \cdot (n_{0.5})^{c \cdot (T_o - T) + d}. \quad (1)$$

64 Here T is the temperature in the section of the CFDC operated above water saturation,
65 T_o is the reference temperature adopted by D10 (273.16 K, their Eqn. 1), and a, b, c and
66 d are the fitted coefficients. We reexamine Eqn. 1 because it was developed with the
67 CFDC operating in a manner which restricted the upper-limit diameter of aerosol
68 particles processed within the CFDC (D < 1.6 µm) and which restricted the duration of
69 the particle's exposure to water-saturated conditions (t < 10 s). Since both of these
70 restrictions can cause INP concentrations to be underestimated (D10; Wright et al., 2013;
71 DeMott et al., 2015), we use measurements made in and near clouds to evaluate the
72 potential bias.

73 We have three specific objectives. First we use our airborne measurements of IC
74 concentration to derive a temperature-dependent fit of those measurements. We refer to
75 these two properties as N_{IC} and $N_{IC}(T)$, respectively. Specifically, we analyze IC
76 concentrations recorded within the downwind (descending flow) portion of middle-
77 tropospheric wave clouds, where IC concentration is thought to reflect INP activation that

78 occurred upwind, within the colder and liquid-water saturated portion of the cloud.
79 Second, we use our measurements to derive a temperature- and aerosol-dependent fit of
80 N_{IC} based on Eqn. (1). We refer to the latter as $N_{IC}(T, n_{0.5})$. Third, we analyze our
81 measurement of N_{IC} with an estimate of the interval of time an air parcel was exposed
82 to water-saturation within a wave cloud. This is relevant to cloud modeling because many
83 models employ a state- and time-dependent framework to predict IC concentration [e.g.,
84 Hoose et al., 2010]. The INP, aerosol and IC concentrations relevant to our work are
85 summarized in Tab. 1.
86 The foundations of our investigation are the cold-season middle-tropospheric
87 wave cloud studies of Cooper and Vali (1981), Cotton and Field (2002), Eidhammer et al.
88 (2010) and Field et al. (2012). The prior research demonstrated that an assessment of
89 wave cloud kinematics can be used to distinguish heterogeneous from homogeneous
90 nucleation and that crystal production occurs primarily via the previously mentioned
91 freezing nucleation pathways. Further, no compelling evidence for secondary ice
92 production was reported in those prior studies.
93 Our investigation is most similar to the airborne studies of Eidhammer et al.
94 (2010) and Field et al. (2012). Those authors analyzed cold-season (late fall)
95 measurements made near, and within, wave clouds during the ICE-L project conducted in
96 2007. Their measurements were made over northern Colorado and southern Wyoming.
97 Our work is based on cold-season airborne measurements made during the Wyoming
98 Airborne Integrated Cloud Observation (WAICO) study conducted 2008 and 2009 [Wang
99 et al., 2012]. We analyze measurements made at locations where a streamline model
100 indicated our aircraft intersected air that ascended into, and descended from, wave

clouds. As we will discuss in detail, we develop a data set from eight flights; 80 wave cloud streamlines are analyzed. In contrast, Eidhammer et al. (2010) analyzed data from one flight, and modeled three streamlines. Field et al. (2012) expanded that analysis, and reported on measurement/model comparisons for 28 streamlines. In their analyses, both Eidhammer et al. (2010) and Field et al. (2012) exercised a streamline-following aerosol and cloud microphysical parcel model, and both derived the model's initial thermal state using measurements made downwind of the investigated wave clouds. In contrast, we use a streamline model to track the evolution of bulk thermodynamic properties (parcel microphysics is not evaluated), and we use thermodynamic measurements made immediately upwind of the investigated clouds, within ascending air, to initialize the model.

2 - Measurements

All measurements were acquired onboard the University of Wyoming King Air [Wang et al., 2012]. The base of operations was Laramie, Wyoming. All of the sampled clouds were in the altitude range 3700 to 7400 m, and were located north of Laramie, within 110 km.

2.1 - Temperature and Humidity

Temperature (T) was measured using a reverse-flow immersion thermometer [Lawson and Cooper, 1990]. Dew point temperature (T_{dp}) was derived from vapor density measurements made with a LI-COR gas analyzer (model LI6262). The latter is characterized by a 0.2 s time response [Dobosy et al., 1997] and this value is somewhat smaller than the time response of the reverse-flow temperature sensor [~1 s; Rodi and Spyers-Duran, 1972]. The inlet to the LI-COR was forward-facing and was operated

subisokinetically with its inlet airspeed set at approximately 18 m/s. The latter is a factor of six smaller than the airspeed of the King Air (110 m/s).

2.2 - Microphysics

Three wing-mounted optical particle counters are used in this analysis: 1) the Passive Cavity Aerosol Spectrometer Probe (PCASP), 2) the Forward Scattering Spectrometer Probe (FSSP), and 3) the Two Dimensional Optical Array Probe (2DC). Each of these was fabricated by Particle Measuring Systems (PMS; Boulder, CO).

The PCASP was used to measure the concentration of particles with diameters between 0.12 μm to 3.2 μm. Particle sizing was based on laboratory calibrations conducted using monodisperse test particles with refractive index n = 1.59 [Cai et al., 2013]. PCASP concentrations were derived as the ratio of particle count rate divided by a calibrated sample flow rate [Cai et al., 2013].

Adiabatic compression warms the aerosol stream as it approaches the PCASP inlet. Strapp et al. [1992] estimated that this process occurs over 0.2 s. Once the stream reaches the probe, it is warmed by three anti-ice heaters (Particle Measuring Systems, 2002). The time scale for diabatic (anti-ice) heating is approximately an order of magnitude smaller than the adiabatic warming. Because of both the adiabatic and diabatic processes, unactivated cloud droplets (haze particles), and cloud droplets, are partially evaporated prior to sizing within the PCASP. In the case of haze particles, evaporation is complete if the initial particle diameter is smaller than ~1 μm [Strapp et al., 1992; Snider and Petters, 2008].

The FSSP was used to categorize cloud droplets sizes from 1.5 to 47.5 μm into 15 bins. During WAICO the cloud droplet concentrations were less than 300 cm^{-3}, so the

148 FSSP dead time and coincidence errors are less than 25 % [Baumgardner et al., 1985].
149 Both of these effects were accounted for in the data processing. Because our FSSP
150 measurements come from clouds containing ice, bias due to ice crystal shatter also needs
151 to be addressed. Since we only analyze FSSP measurements recorded near the upwind
152 edge of the clouds, where the ice crystals are small (< 100 μm) and their concentration is
153 low (< 0.4 L^{-1}), the effect of shatter on the FSSP measurements is not expected to be
154 significant [Gardiner and Hallett, 1985; Gayet et al., 1996; Field et al., 2003] and was not
155 evaluated.

156 Ice crystals were sized and counted using an optical array probe (2DC) [Pokharel
157 and Vali, 2011]. This instrument records a crystal as a two-dimensional image. Some
158 images were rejected using criteria described in Pokharel and Vali [2011]. Images which
159 passed the rejection tests were sized in the along-track direction (hereafter, this dimension
160 is termed "diameter") and these were binned into channels with lower-limit diameters set
161 at 25, 50, 100, 150, 200, 250, 300, and 400 μm for the smallest eight of 20 channels;
162 nearly all crystals recorded during WAICO classified into these eight channels. Because
163 even the largest crystals in this set are smaller than the size known to shatter when
164 impacted at aircraft velocities [Korolev and Isaac, 2005; Korolev et al., 2013], the effect
165 of shatter was ignored. Concentrations were derived by assuming that the optical depth of
166 field, for all crystals and regardless of their size, was equal to the 2DC's sampling
167 aperture (61 mm) [Vali et al., 1981]. Crystal concentration and crystal interarrival time
168 measurements, derived using the 2DC, are analyzed in greater detail in Appendix A.

169 2DC-derived concentrations were validated by Cooper and Saunders (1980). The
170 basis for their validation was airborne 2DC concentrations measured simultaneous with

concentrations derived by impacting ice crystals onto oil-coated slides (OCS) exposed in a decelerator. Crystals impacted on the slides were photographed and counted, the counts were increased by dividing by a size-dependent impaction efficiency, and diameter-integrated concentrations were computed for crystals with maximum dimension larger than 50 μm. The OCS concentrations were compared to 2DC concentrations. The latter were derived by integrating from 50 μm to larger diameters. Cooper and Saunders reported 2DC-OCS concentration ratios between 3.6 and 0.6 ($\bar{x}$ = 1.7, σ = 0.9, number of samples = 12). From the comparisons it was concluded that, for crystals larger than 50 μm, the 2DC is capable of making quantitative concentration measurements.

Based on the findings discussed in the previous paragraph we derived N_{IC} (Tab. 1) as the diameter-integrated concentration corresponding to D > 50 μm. Further, we excluded from our analysis instances when the concentration of crystals in the first 2DC channel (25 to 50 μm) exceeded more than 50 % of the overall (D > 25 μm) diameter-integrated concentration. The intent of this criterion is avoidance of crystals whose concentration is uncertain because their depth of field is ambiguous. If we had summed those crystals into N_{IC}, the relative concentration bias could have approached a limiting value equal to the ratio of the 2DC manufacturer's recommendation for a 25 to 50 μm particle's depth of field (~4 mm) divided by the sampling aperture (61 mm) [Strapp et al., 2001].

For both the PCASP and the 2DC, the relative Poisson sampling error was evaluated as the reciprocal of the square root of particle count.

193 **2.3 – Air Motion**

194 Vertical and horizontal air velocities were derived from differential pressure
195 measurements made at the tip of the King Air's nose boom [Parish and Leon, 2013].

196 **2.4 - Lidar**

197 The upward-pointing Wyoming Cloud Lidar [Wang et al., 2009; Wang et al.,
198 2012] was used to remotely sense cloud boundaries. The lidar transmits in the near
199 ultraviolet (λ = 0.355 μm) at a pulse repetition frequency of 20 Hz. Seven lidar shots
200 were averaged, making the time between samples 0.35 s. The vertical resolution of the
201 lidar is 3.75 m. Using the lidar measurement of attenuated backscatter and depolarization,
202 we evaluated the boundaries between clear air and liquid cloud, and between liquid-
203 dominated and ice-dominated cloud (Wang and Sassen, 2001).

204 In the next section we describe our determinations of the air parcel streamlines
205 and how the lidar-derived cloud boundaries were used to evaluate the time interval, along
206 the streamlines, within the liquid-dominated portions of the clouds.

207 **3 - Analysis**

208 **3.1 - Parcel Streamlines and Parcel Thermodynamic State**

209 Here we explain how the streamlines were derived from measurements made
210 during level-flight penetrations of 35 wave clouds. In our data set we have 19
211 penetrations made along the wind, and sixteen penetrations made against the wind. Also
212 described is the parcel model we used to evaluate thermodynamic properties along the
213 streamlines.

214 An average horizontal wind speed ($\bar{u}$) was derived from airborne in-situ wind
215 measurements made during each of the cloud penetrations. That average was applied as a

constant in our streamline analysis. In contrast, the in-situ measured vertical wind component (w) was oscillatory, so we fitted it as a sinusoid function, versus along-track distance (x), and we assumed that the fitted vertical wind component ($w(x)$) did not vary vertically. Fig. 1a shows the measured and fitted values of the vertical wind for a penetration that we showcase to illustrate our methods.

Within the ascending portion of the wave structure (e.g., to the left (upwind) of x = 10.5 km in Fig. 1a), we initialized several streamlines. The streamline center points were separated by ~ 550 m along the flight track (five seconds at 110 m/s). For each of the center points the 1 Hz measurements of T , T_{dp}, and pressure (P) were used to derive five-second averaged values of T , T_{dp}, and P . These three properties were used to fix an air parcel's initial thermodynamic state. A closed parcel model, conserving potential temperature below the lifted condensation level (LCL), and equivalent potential temperature, above the LCL, was used to evaluate the thermal state, along a streamline. Using this model, and the aforementioned descriptions of the horizontal and vertical wind components, we simulated the thermal and kinematic evolution of streamline-following air parcels. One of the evaluated relationships is the parcel's temperature as a function of the along-track distance. An example of this is shown in Fig. 1d. Also indicated are the minimum streamline temperature (T_{low}) and the measurement of temperature (red circle) made at the downwind intersection of the flight track and the streamline.

We compared our streamline temperatures, each evaluated at the downwind track-streamline intersections, and the corresponding measured temperatures. The average absolute difference is 0.3 ^{o}C (number of samples = 80). This agreement is consistent with a small effect, smaller than the temperature measurement error (±0.5 ^{o}C), coming from

239 violations of either the closed parcel assumption or the assumptions of vertically-uniform
240 $w(x)$ and constant $\bar{u}$.

241 **3.2 - Mixed-phase Time**

242 The interval of time an air parcel experiences water-saturated conditions was
243 evaluated by combining the lidar measurements with the streamline information. We refer
244 to this time interval as the mixed-phase time (t_{MP}). Figs. 1b and 1c illustrate how t_{MP}
245 was evaluated. At the upwind cloud edge, at x = 9.5 km but above the aircraft, the
246 streamline encounters the first of two cloud boundaries. Using lidar measurements, we
247 defined this upwind cloud boundary by its increased lidar backscatter and decreased lidar
248 depolarization (compared to the depolarization in clear air). Approximately four
249 kilometers downwind, the streamline encounters the second boundary. We defined this
250 boundary by its decreased lidar backscatter and increased depolarization. Here the
251 boundary is between liquid- and ice-dominated cloud. Further, we defined t_{MP} as the
252 integral of the parcel transit time between these two boundaries. For a few of the
253 streamlines, the downwind track-streamline intersection was within the liquid-cloud
254 region. In those cases, the calculation of t_{MP} was stopped at the intersection. The lower
255 and upper bounds of t_{MP} are 38 to 507 s; the average t_{MP} is 221 s.

256 We obtained good agreement between values of t_{MP}, based exclusively on lidar,
257 and those based partially on the in-situ measurements of T and T_{dp}. These comparisons
258 were made by differencing the lidar-derived t_{MP} and a mixed-phase time derived using
259 T- and T_{dp}-dependent determinations of the LCL (Sect. 3.1) combined with lidar-based
260 determinations of the downwind cloud boundary. In this comparison the average absolute

difference is 22 s. Each absolute difference was converted to a relative difference by dividing by the lidar-derived values of t_{MP}. The relative differences range from 0.0 to 0.9.

3.3 - Aerosol Particles and Cloud Droplets

In this section we evaluate aerosol concentrations and compare to in-cloud droplet concentrations. For each of the 35 cloud penetrations we evaluated five-second averages of the PCASP and FSSP concentrations. For the PCASP, the averaging interval was started five seconds upwind of the cloud, and for the FSSP, the averaging interval was started at the cloud edge. Averaging intervals are shown at the bottom of Fig. 2b and at the top of Fig. 2d. Also presented (Figs. 2a, 2b and 2c) are the size-resolved concentrations from the PCASP, FSSP and 2DC. The series shown in Fig. 2 are for the same section of flight illustrated in Fig. 1.

Similar to Eidhammer et al. [2010], we compared the upwind aerosol particle concentration (D > 0.25 μm; five-second averaged) to the in-cloud droplet concentration (D > 1.5 μm; five-second averaged). From the series presented in Fig. 2d, it can be seen that droplets, measured at ~ x = 11 km (i.e., downwind of the cloud edge), were more abundant than aerosol particles measured at ~ x = 10.5 km (i.e., upwind of the edge). Following this same averaging procedure, we evaluated a droplet-to-aerosol ratio for 32 of our 35 penetrations; three of the 35 were discarded because droplets were smaller than the minimum size detectable by the FSSP (D = 1.5 μm). In the 32 comparisons, the droplet-to-aerosol concentration ratios were consistently greater than 0.7. These results are consistent with the findings of Eidhammer et al. [2010]. A reasonable inference is that the D > 0.25 μm particles are internally mixed, that the mixture's water-soluble fraction

promoted the nucleation of the droplets, and that the mixture's water-insoluble fraction promoted ice nucleation, presumably via the condensation and immersion freezing pathways. The effect of ice development on cloud properties is evident at the downwind track-streamline intersection in Figs. 1 and 2. Most noticeable are the enhanced lidar depolarization ratios seen at x ≥ 15 km in Fig. 1c and the enhanced diameter-integrated crystal concentrations seen at x ≥ 15 km in Fig. 2d.

3.4 - D > 0.5 μm Aerosol Particle and IC Concentrations

In addition to the D > 0.25 μm aerosol concentrations, analyzed in the previous section, we also evaluated $n_{0.5}$ (Sect. 1). These were averaged outside of cloud during the five-second time windows used for thermodynamic-property averaging (Sect. 3.1). For the rest of the paper, $n_{0.5}$ is reported as a particle count per standard cubic centimeter ($sccm^{-1}$). Also for the rest of the paper, values of N_{IC} (Tab. 1) are derived as five-second averages evaluated at the downwind track-streamline intersections (e.g., at ~ x = 15 km in Fig. 1c), and these are reported as a crystal count per standard liter (sL^{-1}).

3.5 - Data Set

In the previous sections we described how values of N_{IC}, $n_{0.5}$, T_{low}, and t_{MP} were evaluated for each streamline. The subset $\{N_{IC}, n_{0.5}, T_{low}\}$ is the streamline data we used to develop a fit of N_{IC}, according to the mathematical form of Eqn. 1. However, before fitting our measurement data, we excluded streamlines affected by four effects: 1) an abundance of crystals in the first 2DC channel, 2) homogeneous freezing, 3) crystal sublimation, and 4) variable aerosol particle and crystal concentrations. Conditions for data *inclusion* are: (1) N_{IC}(D<50μm) must be smaller than

306 $0.5 \cdot N_{IC}(D>25\mu m)$ (Sect. 2.2); 2) T_{low} > -35 °C [Heymsfield and Miloshevich, 1993]; 3)
307 ice saturated, or larger relative humidity, at the downwind track-streamline intersection;
308 and 4) relative Poisson sampling errors (Sect. 2.2) less than specified thresholds [1]. Out of
309 the 116 streamlines we analyzed, 80 satisfy our data inclusion criteria. The set
310 $\{N_{IC}, n_{0.5}, T_{low}, t_{MP}\}$ is provided for the 80 streamlines in the supplementary
311 information.

312 **4 – Fitted N_{IC} Equations**

313 In this section we show results from fitting our measurement data with both
314 temperature-dependent, and temperature-aerosol-dependent, equations. We start with a
315 solely temperature-dependent fitting equation because many previous cloud modeling
316 studies were based on such a relationship [e.g., Meyers et al., 1992], and because the rate
317 of change of crystal concentration with temperature can have a profound impact on
318 modeled cloud properties [Eidhammer et al., 2009].

319 We develop the fitting equations using logarithm-transformed crystal and
320 logarithm-transformed aerosol concentrations. The reason for log-transforming the data is
321 that we expect errors, in both crystal and aerosol concentration, to be multiplicative in the
322 sense that larger values correspond with larger error and vice versa. Multiplicative error,
323 scaling in proportion to the square root of concentration as predicted by the Poisson
324 probability law [Young, 1962; Rogers and Yau, 1989], was documented by Cai et al.
325 (2013) in their investigations of the PCASP's response to steadily-generated
326 monodisperse test particles.

---

[1] The relative Poisson error thresholds adopted for IC concentration and for $n_{0.5}$, were 0.4 and 0.7, respectively. These values cut the distributions of the relative Poisson errors at their 99th percentiles.

Fig. 3a shows the temperature-dependent fit (i.e., $N_{IC}(T_{low})$) plotted versus measured N_{IC}. The square of the Pearson correlation coefficient (r^2), for this scatter plot, is relatively small and demonstrates that temperature alone, via the fit equation, can only explain 51% of the N_{IC} variability.

In Fig. 3b we plot the temperature- and aerosol-dependent fit $N_{IC}(T_{low}, n_{0.5})$ versus measured N_{IC}. Results shown here are for one of two fitting methods we implemented. In fit method #1 we used the Matlab Curve Fitting Toolbox (The MathWorks, Natick, MA), with the log-transformed version of Eqn. 1, and derived the logarithm of a ($\ln a$), and the values of b, c and d. We also fitted the set $\{N_{IC}, n_{0.5}, T_{low}\}$ using the using the three-step procedure described in D10. We refer to the latter as method #2 and describe our implementation of that method in Appendix B. The advantage of method #1 is that it shortens D10's three-step procedure to one step.

The fit coefficients derived by D10, our fit coefficients (methods #1 and #2), and the method #1 and #2 statistical errors, expressed as standard deviations, are presented in Tab. 2. Focusing on results obtained using method #1, our four coefficients are seen to agree within two standard deviations of D10's. Also, agreement within two standard deviations was obtained between our application of method #2 and D10's.

By inputting the statistical errors from Tab. 2 into a propagation of error equation (Young, 1962; their Eqn. 13.9), we evaluated contributions to the relative variance of the logarithm of $N_{IC}(T_{low}, n_{0.5})$ (method #1). For $n_{0.5} \leq 3.4$ sccm^{-1} (the average for our data set), and for temperatures over the full range of our data set ($-34 \leq T_{low} \leq -14$ ^{o}C), the relative variance is controlled by terms proportional to both the square of the

statistical error in $ln\,a$ and the square of the statistical error in b. Further, we also evaluated the fractional standard deviation of $N_{IC}(T_{low}, n_{0.5})$ (method #1). For the same $n_{0.5}$ and T_{low} settings provided above, the fractional standard deviation is ~ 4 and increases to ~ 5 if $n_{0.5}$ is set to 16 sccm^{-1} (the maximum for our data set). Yet, in spite of this uncertainty, our fitted (method #1) and measured values are seen to correlate over IC concentrations that range from 0.1 to 100 sL^{-1} (Fig. 3b). Also illustrated are fitted concentrations, derived using Eqn. 1 with D10's coefficients, and our measurements of T_{low} and $n_{0.5}$. In either case the r^2 is ~ 0.7 and thus larger than that for the temperature-only fit (cf., Fig. 3a).

We also evaluated the fraction of the measured crystal concentrations that plot within a factor of two of the fit. Based on our method #1 coefficients, this percentage is 69% and thus larger than the percentage (66 %) based on fit coefficients from D10 (the percentage is 71% when using the method #2 coefficients; not shown here). Thus, we obtained better fitted-vs.-measured agreement with our method #1 and method #2 fit coefficients and somewhat poorer agreement with the D10 coefficients.

5 – Effect of Mixed-phase Time

As was discussed in the introduction, there is an outstanding question in atmospheric science community regarding the time-dependent nature of ice nucleation. Of relevance for our data set, with its average t_{MP} =221 s (Sect. 3.2), is the possibility that the characteristic time for an embryo to transition to a crystal is comparable to t_{MP}. If that were the case, we would expect that streamlines associated with larger mixed-phase times, all other relevant properties the same, would have larger IC concentrations. The

371 work of Vali and Snider (2015) provides an estimate the effect. They show that time
372 dependency can alter crystal concentrations by up to a factor of three depending on
373 whether a time- and temperature-dependent parameterization or purely temperature-
374 dependent parameterization is used to describe heterogeneous ice nucleation.

375 We investigated time dependency by stratifying our 80 determinations of {N_{IC},
376 $n_{0.5}$,T_{low}, t_{MP}} into four T_{low} subsets. In Tab. 3 we present the subset's minimum and
377 maximum temperatures, the averaged $n_{0.5}$, and the number of data values. For each of
378 these we tested the hypothesis that $ln(N_{IC})$ is correlated with $ln(t_{MP})$. Values of the
379 Pearson correlation coefficients (r), and the levels of significance (p), demonstrate that
380 none of the correlations are significant (i.e., all have $p > 0.05$). This same conclusion was
381 reached after removing from the correlations those points exhibiting the largest t_{MP}
382 uncertainty (relative difference > 0.3, Sect. 3.2), but those results are not shown in Tab. 3.
383 We also stratified by $n_{0.5}$ within the four T_{low} subsets. One of those correlations
384 ($ln(N_{IC})$ versus $ln(t_{MP})$) approaches statistical significance, with $p = 0.1$ and with 10
385 paired values; the rest have $p > 0.1$. That subset plots in the gray rectangle shown in Fig.
386 4a and the N_{IC} versus t_{MP} correlation for that subset is shown in Fig. 4b.

387 In spite of these suggestions of a connection between crystal concentration and
388 mixed-phase time we cannot argue convincingly that time-dependent effects were
389 significant for crystals within the clouds we studied. Our ability to argue for, or against a
390 dependence on t_{MP}, was limited by the strong temperature-dependence of ice nucleation.
391 This is evident from Fig. 3a where the value $k_2 = -0.22\ ^{o}C^{-1}$ can be used to demonstrate
392 that a 5 ^{o}C decrease corresponds to a factor of three increase in nucleated concentration.

Also limiting are the relatively few data values within our 5 ^{o}C subsets. Thus, in future wave cloud studies, attention should be paid to strategies which generate an adequate number of points within specified temperature and aerosol ranges.

6 – Summary and Conclusion

The result we present in Tab. 2, with fit coefficients generally consistent, in a statistical sense, with those reported by D10, is important because it validates D10's approach using different methodology. In short, we use a streamline model to connect a measurement of aerosol concentration ($n_{0.5}$), made upwind of a wave cloud, to a downwind measurement of IC concentration. Our reconfirmation of the relationship between crystals and $n_{0.5}$, implied by Eqn. 1, is conceptually appealing because it acknowledges that aerosol particles are necessary for the occurrence of heterogeneous ice nucleation. Appeal also comes from the linkage provided by Eqn. 1, through aerosol, to cloud processes.

We also probed the conjecture that the duration of INP exposure to water-saturated conditions is a determinant of IC concentration. Our analysis shows no statistically-robust evidence for this. This finding is relevant to descriptions of ice nucleation within water-saturated layer clouds (e.g., stratocumulus and altostratus) where temperature is relatively uniform, and steady, and where time-dependent ice nucleation is suspected of occurring continuously and with substantial meteorological impact [Crosier et al., 2011; Westbrook and Illingworth, 2013]. In fact, many model representations of heterogeneous nucleation anticipate this time-dependent, constant-temperature, phenomenon. Also, in some models, the nucleation rate is set to zero when the temperature tendency is zero or positive [Khain et al., 2000; Muhlbauer and Lohmann,

2009], but this action is not supported by all of the experimental evidence currently available (for a review, see Vali (2014)). Further investigation is needed to confirm our conclusion of little, if any, time-dependent effect within the cloud type we studied (middle-tropospheric wave clouds). Going forward, we anticipate our methodology will help advance understanding of time-dependent atmospheric ice nucleation, and atmospheric ice nucleation in general.

Appendix A

In this appendix we examine the reliability of ice crystal concentrations derived using the University of Wyoming 2DC. We derive concentrations using the Wyoming 2DC, with its slower-responding photodiode array (Gayet et al., 1993; Baumgardner and Korolev, 1997; Strapp et al., 2001), and compare to values derived using a faster responding cloud imaging probe (CIP; Baumgardner et al., 2001). We also analyze the 2DC ice crystal interarrival times and investigate crystal shattering. Two data sets are analyzed. The first comes from Wyoming King Air flight data, acquired on 9 January 2011 during the Colorado Airborne Multi-Phase Cloud Study (CAMPS), and the second comes from the 80 downwind track-streamline intersections described in Sect. 3.5. Both the 2DC and CIP were operated with standard probe tips (Korolev et al., 2013).

Strapp et al. (2001) conducted laboratory studies that investigated a 2DC's ability to detect objects (circular dots) positioned away from the center of focus of the probe's laser. They demonstrated that the probe's finite response led to undersizing, counting losses and image distortion. In the case of dot sizes smaller than 100 μm, undersizing and counting losses increased with the speed the dots transited through the probe's sample volume. Strapp et al. conducted their testing using dots deposited onto a glass disk. The dots were opaque, monodisperse, and regularly spaced on the disk along circular tracks. The disk was positioned with its rotational axis parallel to the 2DC laser beam. The position of the disk plane, relative to the center of focus of the beam, was varied. The largest dot speeds tested by Strapp et al. were comparable to the airspeed of the Wyoming King Air (~100 m/s).

446 **A1 - 2DC and CIP Concentrations**

447 A comparison of 2DC- and CIP-derived concentrations was made using Wyoming
448 King Air data acquired on 9 January, 2011 (20110109). The comparison data was selected
449 from three level-flight transits of an orographic cloud. The cloud was located over
450 continental divide in northern Colorado. During the cloud transits the liquid water content
451 was less than 0.2 g m^{-3} and temperature was between -23 and -25 ^{o}C. We processed the
452 raw 2DC and CIP measurements the same way we processed the WAICO 2DC
453 measurements (Sect. 2.2). Also consistent with the WAICO processing, the compared
454 concentrations are five-second averages and are for crystals larger than 50 μm (sized
455 along the aircraft track). The CIP/2DC comparison is shown in Fig. A1a. The vertical line
456 at 5 L^{-1} marks the median of the 80 concentrations in our WAICO data set (Sect. 3.5), and
457 its implication is discussed in the following paragraph.

458 Because of the undersizing and counting losses documented for a 2DC, especially
459 at the low end of its range (D < 100 μm), and the fact these effects are attributed to the
460 relatively slow time response of the 2DC's optical array (Strapp et al., 2001), we expected
461 that concentrations derived using the faster responding CIP (Baumgardner et al., 2001)
462 would exceed 2DC-derived values. Contrary to that expectation, we found reasonable
463 agreement (Fig. A1a). Measures of the agreement are as follows: 1) For concentrations
464 larger than 5 sL^{-1}, all of the 2DC-derived values plot well within a factor of two of the
465 CIP. 2) For concentrations smaller than 5 sL^{-1}, a large fraction of the 2DC values (87%)
466 plot within a factor of two of the CIP. These findings, combined with the findings of
467 Cooper and Saunders (1980) (also see Sect. 2.2), lend confidence to the concentration
468 values we derived using 2DC measurements made during WAICO. However, this

469 comparison does not completely lessen the concern that we biased the WAICO
470 concentrations at D < 100 μm by assuming that the 2DC's optical depth of field was
471 independent of crystal size and equal to the probe's sampling aperture (61 mm) (Vali et
472 al., 1981 and Sect. 2.2).

473 **A2 - Interarrival Time and Shattering**

474 Representative CIP and 2DC size distributions, from CAMPS, are shown in Fig.
475 A1b. It is evident that most of the detected crystals are smaller than 400 μm, especially in
476 the 2DC measurement. A size distribution from one of the 80 WAICO downwind track-
477 streamline intersections is shown in Fig. A2a. The largest crystal detected in this five-
478 second interval is 400 μm. The figure also demonstrates that the diameter-integrated
479 concentrations N_{IC}(D>100μm) and N_{IC}(D>50μm) are comparable, and that the ratio
480 N_{IC}(D>100μm)/N_{IC}(D>50μm) is only somewhat smaller than unity; for our 80 size
481 distributions the average ratio is 0.7.

482 A histogram of crystal interarrival times from WAICO is shown in Fig. A2b.
483 Evident in the left tail of the histogram is a minimum, at interarrival time $\tau^* = 2\text{x}10^{-3}$ s,
484 where we delineate between a fragment mode ($t < \tau^*$) and a mode corresponding to
485 intact crystals ($t > \tau^*$). We note that only 7% of the crystal counts classify as fragments
486 and that this fraction is much smaller than the example presented by Korolev et al. (2013)
487 for a 2DC with standard probe tips (their Fig. 14a).

488 We analyzed interarrival times obtained from each of the 80 WAICO downwind
489 track-streamline intersections. Histograms were binned as in A2b (3.5 bins per decade)
490 and all particle images, including those that did not pass the rejection criteria of Pokharel
491 and Vali (2011) (Sect. 2.2), were used. We developed a procedure that searches the

492 histogram for a minimum between $t = 10^{-6}$ s and the histogram mode. In our set of 80
493 there are 16 cases that do not exhibit a minimum and 21 with a provisionally significant
494 minimum. The provisional cases were characterized by a cumulative fraction, evaluated
495 at the minimum, greater than 20%. The example shown in Fig. A2b is not a provisional
496 case because the cumulative fraction at $\tau^* = 2\text{x}10^{-3}$ s is less than 20%. All of the
497 provisional cases exhibited a minimum that was within an order of magnitude of the
498 histogram mode. Because order-of-magnitude separation is substantially less than the
499 minimum-to-mode separation seen Korolev et al. (2013) (their Fig. 14), we concluded
500 that a fragment mode could not be discerned. Thus, we ignored the effect of shattering.
501 Twenty six of the remaining 43 cases (43=80-16-21) had a minimum more than an order
502 of magnitude smaller than the histogram mode; Fig. A2b is an example. For these we
503 ignored the effect of shattering because the fraction affected was less than 20% and
504 because the rejection criteria of Pokharel and Vali (2011) removes some of the affected
505 crystals from the population used to evaluate the concentration.
506

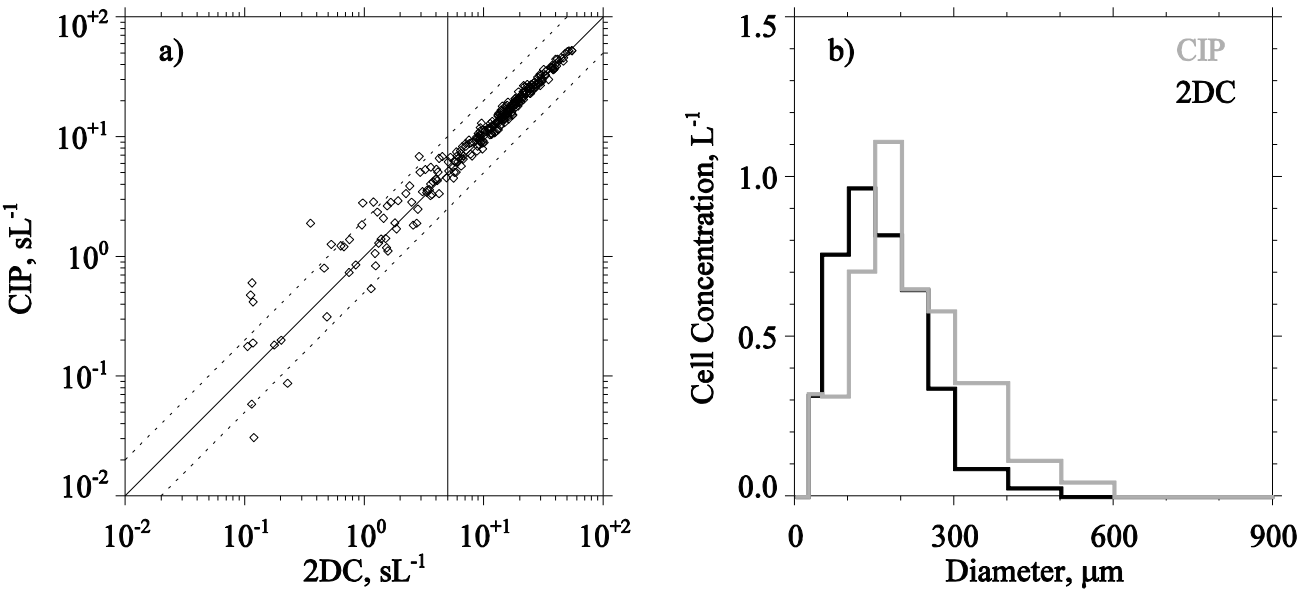

Fig. A1 – a) The CIP/2DC concentration comparison. Compared values are five-second averages and are for crystals larger than 50 µm. Comparison data is from 20110109 during the Colorado Airborne Multi-Phase Cloud Study (CAMPS). Wyoming King Air data shown here was selected from three along-wind level-flight cloud transits: 1) 221200 to 222200 UTC, 2) 223900 to 224800 UTC, and 3) 230600 to 231600 UTC. The vertical line at 5 sL^{-1} is drawn at the median value for our set of 80 WAICO 2DC-derived measurements. b) 2DC and CIP size distributions from a representative five-second subset (224646 to 224650 UTC) of the flight on 20110109.

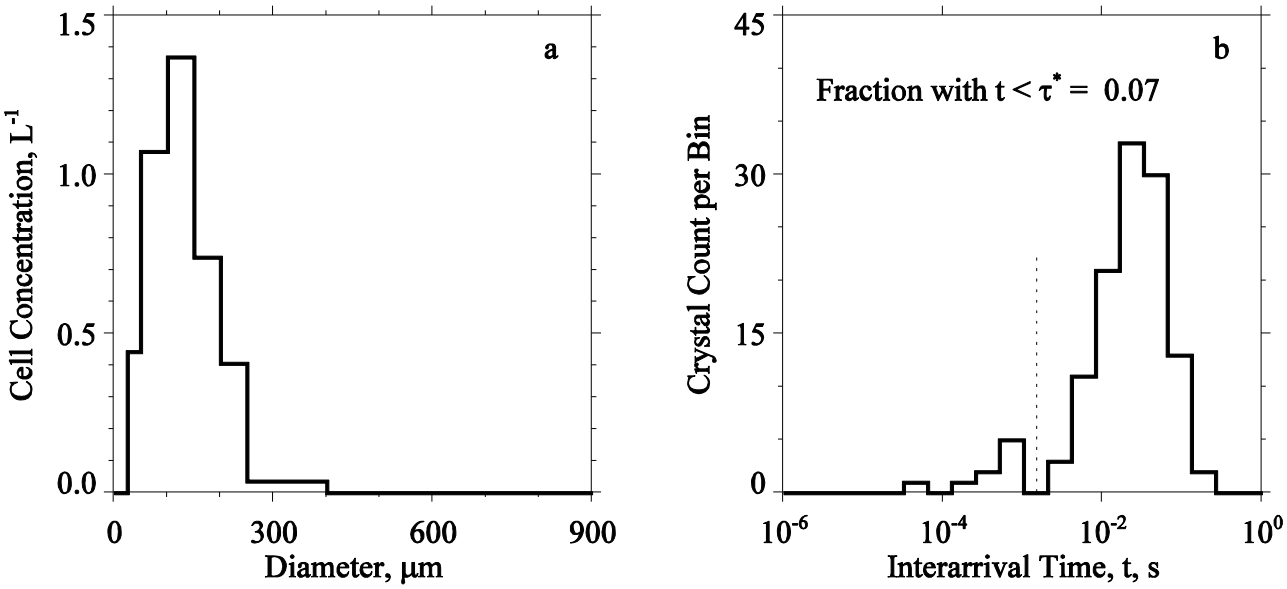

Fig. A2 – a) The 2DC size distribution derived for the WAICO 181933 to 181937 interval on 20080227. This interval corresponds to the downwind track-streamline intersection at x=15 km in Fig. 1c. b) The interarrival time histogram for the 181933 to 181937 interval on 20080227. The vertical dashed line marks a minimum between a fragment mode ($t < \tau^*$) and a mode corresponding to intact crystals ($t > \tau^*$).

Appendix B

Here we describe how we fitted our 80 determinations of the set $\{N_{IC}, n_{0.5}, T_{low}\}$ using the three step procedure developed by D10 (herein method #2). In the first step, the data were binned into four $(273.16 - T_{low})$ subsets; the number of samples in the four subsets is provided in Table 3. In the second step, values of $ln(p_i)$ and q_i were derived for each subset by regression. Here "i" indicates the temperature subset and the form of the regression equation is

$$ln(N_{IC,i}) = ln(p_i) + q_i \cdot ln(n_{0.5,i}). \quad \text{(B1)}$$

In the third step, the values of $ln(p_i)$ were regressed vs. $ln(273.16 - T_{low,i})$, and also, the values of q_i were regressed vs. $T_{low,i}$. In these regressions the $T_{low,i}$ is the average of the subset. The slopes and intercepts of these regressions define the method #2 coefficients $ln(a)$, b, c and d

$$ln(a) = \text{intercept}\left(ln(p_i)\ vs.\ ln(273.16 - T_{low,i})\right) \quad \text{(B2)}$$

$$b = \text{slope}\left(ln(p_i)\ vs.\ ln(273.16 - T_{low,i})\right) \quad \text{(B3)}$$

$$c = \text{slope}\left(q_i\ vs.\ (273.16 - T_{low,i})\right) \quad \text{(B4)}$$

$$d = \text{intercept}\left(q_i\ vs.\ (273.16 - T_{low,i})\right). \quad \text{(B5)}$$

7 – Acknowledgements

Data collection and initial analyses were supported by NSF under Award AGS-0645644. The authors thank Alfred Rodi, Jeffrey French, Larry Oolman, Matthew Burkhart and Perry Wechsler for the assistance they provided during the field and analysis phases of the project. The authors also thank Paul DeMott who critiqued an early draft of the paper. Critiques provided by the reviewers are appreciated. JRS acknowledges support from NSF grant AGS1034858.

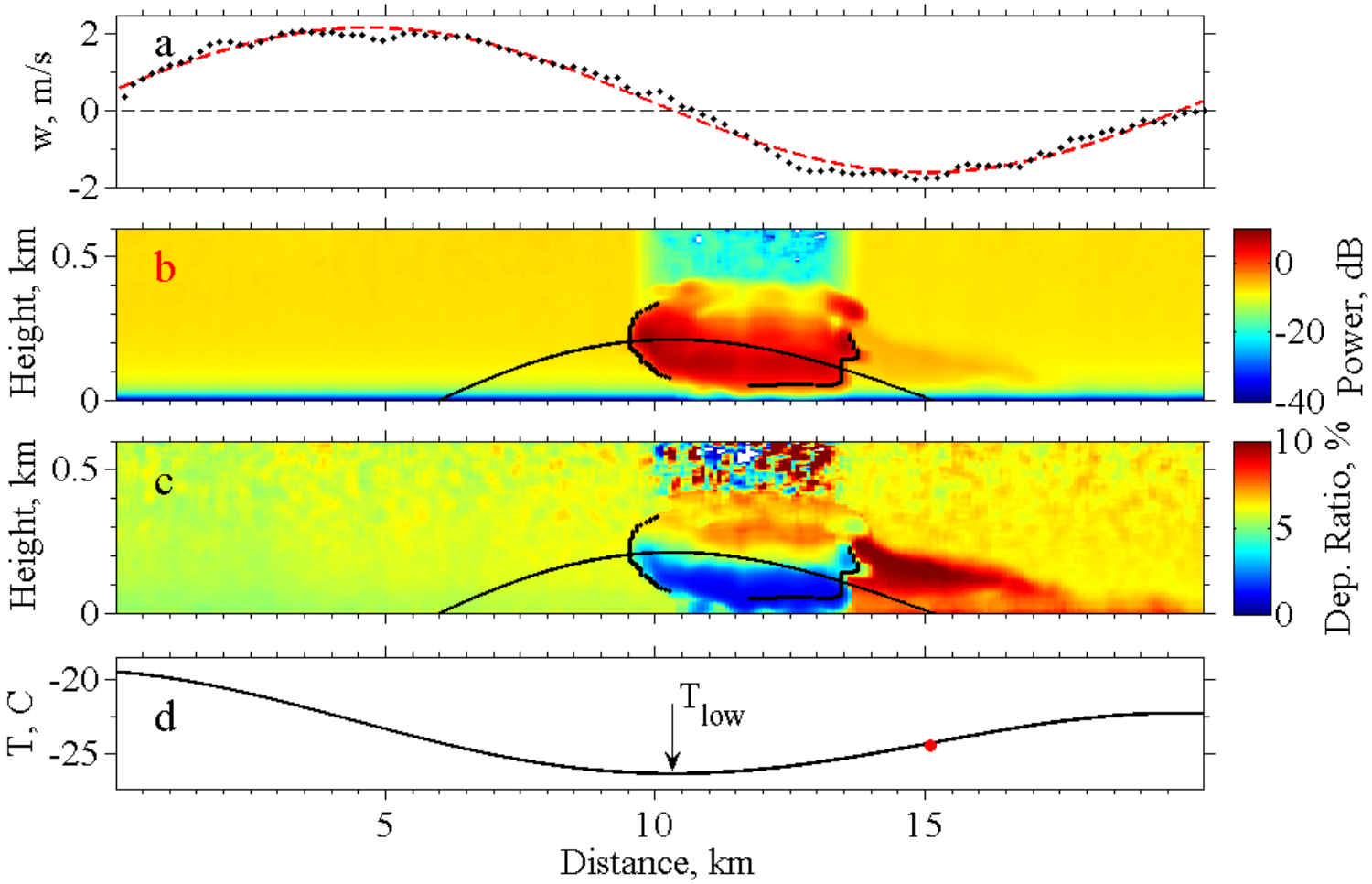

580 Fig. 1. Level-flight sampling a few tens of meter below a wave cloud between
581 18:17:45 and 18:20:09 on February 27, 2008. Airflow is from left to right. (a) In-situ
582 vertical velocity measurements and the sinusoid fit. (b) The example streamline (black)
583 overlain on lidar backscattered power; the two other black lines delineate the liquid-cloud
584 and ice-cloud boundaries discussed in the text. (c) Example streamline overlain on lidar
585 depolarization ratio; the two other black lines delineate the liquid-cloud and ice-cloud
586 boundaries discussed in the text. d) Streamline temperature, minimum streamline

587 temperature, and the in-situ measured temperature at the downwind track-streamline
588 intersection (red circle).
589

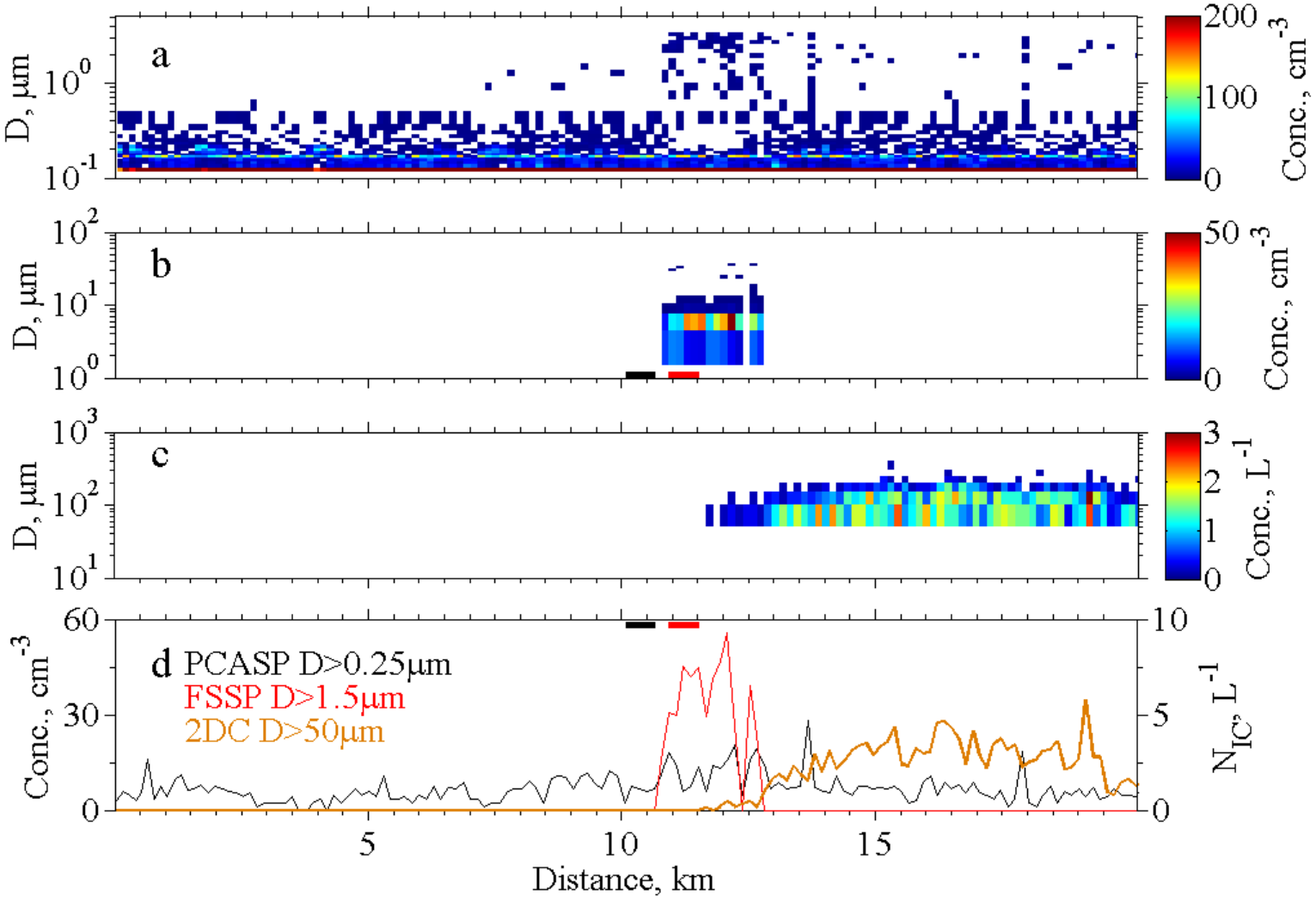

602 Fig. 2. The same segment of flight as shown in Fig. 1. (a) Size-resolved PCASP
603 concentrations. (b) Size-resolved FSSP concentrations. The black and red horizontal
604 rectangles at the bottom of this panel are the five-second averaging intervals for aerosol
605 and droplets analyzed in Sect. 3.3. (c) Size-resolved 2DC concentrations. (d) Diameter-
606 integrated PCASP (D > 0.25 µm, black line), diameter-integrated FSSP (D > 1.5 µm, red
607 line), and diameter-integrated 2DC (D > 50 µm, orange line) concentrations. Averaging
608 intervals for aerosol and droplets are repeated from panel b.

609

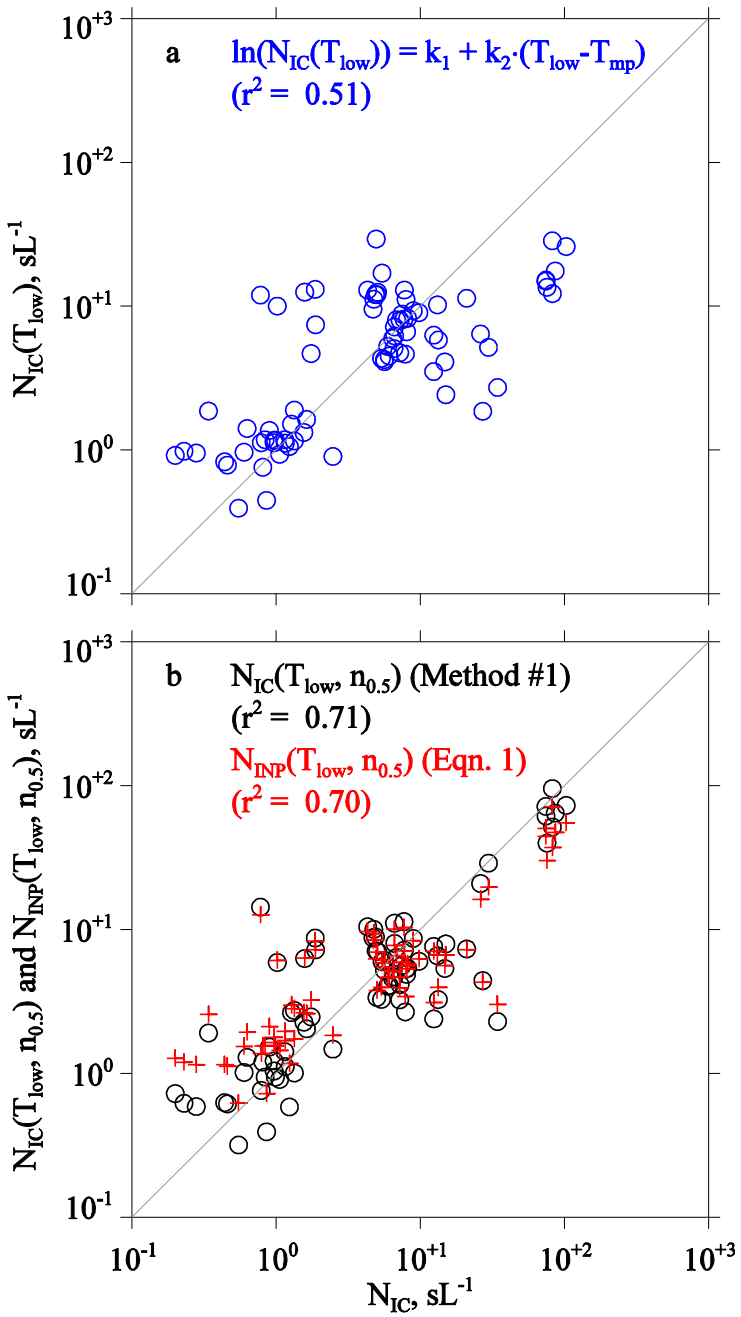

Fig. 3- a) Values of $N_{IC}(T_{low})$ ($\ln(N_{IC}(T_{low})) = k_1 + k_2 \cdot (T_{low} - T_{mp})$ with T_{mp} =273.15 K, k_1 = -4.04 and k_2 = -0.22 $^{o}C^{-1}$) plotted versus measured N_{IC}. b) As in Fig. 3a, but with $N_{IC}(T_{low}, n_{0.5})$ (method #1 fit coefficients), and $N_{INP}(T_{low}, n_{0.5})$ (Eqn. 1), plotted versus measured N_{IC}. In Figs. 3a and Fig. 3b, the square of the Pearson correlation

628 coefficients (r^2) was evaluated using log-transformed concentrations. Also, the one-to-
629 one line is shown in both panels.
630

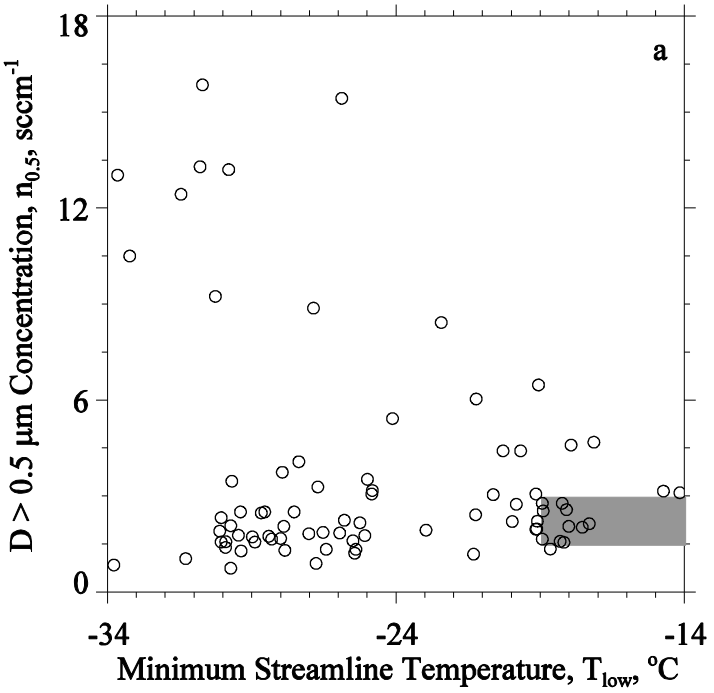

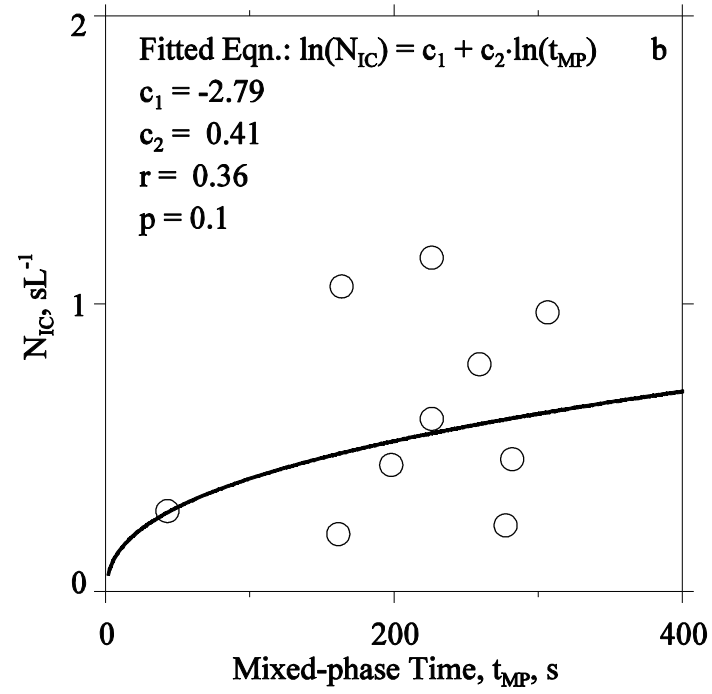

Fig. 4 - a) The 80 paired values of $n_{0.5}$ and t_{MP} in our data set. The gray rectangle highlights the 10 points in the subset defined by -19 ≤ T_{low} < -14 °C and 1.5 ≤

$n_{0.5}$ < 3.0 sccm^{-1}. b) The 10 paired values of N_{IC} and t_{MP} from the gray rectangle shown in Fig. 4a. The black line is the fitting equation $ln(N_{IC}) = c_1 + c_2 \cdot ln(t_{MP})$. The Pearson correlation coefficients (r), and the level of significance (p), were evaluated using the log-transformed concentrations and log-transformed mixed-phase times.

654 Tab. 1 - Symbols used to represent aerosol, INP and IC concentrations
655

Symbol	Definition	Dimension
$n_{0.5}$	Measured aerosol concentration (D > 0.5 µm)	$sccm^{-1}$ [a]
N_{IC}	Measured IC concentration (D > 50 µm) [b]	sL^{-1} [c]
$N_{IC}(T)$	Temperature-dependent fit of IC concentration (see Sect. 4)	sL^{-1}
$N_{IC}(T, n_{0.5})$	Temperature- and aerosol-dependent fit of IC concentration (see Sect. 4)	sL^{-1}
$N_{INP}(T, n_{0.5})$	Temperature- and aerosol-dependent fit of INP concentration (D10) (see Eqn. 1)	sL^{-1}

656

657 [a] Aerosol particle count per standard cubic centimeter at $P=1.013x10^5$ Pa and T=273.15 K

658 [b] 2DC concentration for crystals sizing larger than 50 µm (see Sect. 2.2)

659 [c] Particle count per standard liter at $P=1.013x10^5$ Pa and T=273.15 K

660

661 Tab. 2 - Eqn. 1 fit coefficients

Coefficients	Fit D10 [a]	Fit Method #1	Statistical Error Method #1 [b]	Fit Method #2	Statistical Error Method #2 [c]
ln a	-9.73	-15.26	2.87	-15.03	4.11
b	3.33	4.94	0.88	4.86	1.30
c	0.0264	0.0028	0.0308	0.0038	0.034
d	0.0033	0.86	0.88	0.82	0.83

662

663 [a] Fit coefficients from D10

664 [b] The standard deviations for coefficients fitted via method #1

665 [c] The standard deviations for coefficients fitted via method #2

668

669

670 Tab. 3 - T_{low} subsets and the $ln(N_{IC})$ vs. $ln(t_{MP})$ correlations

T_{min}	T_{max}	$\overline{n_{0.5}}$	Number of samples	r [a]	p [b]
-34	-29	5.50	20	0.20	0.20
-29	-24	2.93	30	0.21	0.14
-24	-19	3.50	15	-0.05	0.57
-19	-14	2.57	15	0.06	0.44

671

672 [a] The Pearson correlation coefficient for the regression of $ln(N_{IC})$ versus $ln(t_{MP})$

673 [b] Level of significance, values of this parameter greater than $p = 0.05$ indicate an
674 insignificant correlation

675

8 - References

Baumgardner, D., W. Strapp and J.E. Dye, Evaluation of the forward scattering spectrometer probe. Part II: Corrections for coincidence and dead-time losses, *J. Atmos. Oceanic Tech.*, 2, 626-632, 1985

Baumgardner, D., and A.Korolev, Airspeed corrections for optical array probe sample volumes, J. Atmos. Oceanic Technol., 14, 1224-1229, 1997

Baumgardner, D., H.Jonsson, W.Dawson, D.O'Connor and R.Newton, The cloud, aerosol and precipitation spectrometer: a new instrument for cloud investigations, Atmos. Res., 59-60, 251-264, 2001

Bigg, E.K., The supercooling of water, *Proc. Phys. Soc. B.*, 66, 688–694, 1953

Braham, R.R. and P.Squires, Cloud Physics-1974, *Bull. Amer. Meteor. Soc.*, 55, 543–586, 1974

Cai, Y., J.R. Snider, and P. Wechsler, Calibration of the passive cavity aerosol spectrometer probe for airborne determination of the size distribution, *Atmos. Meas. Tech.*, 6, 2349-2358, 2013

Cantrell, W., and A. Heymsfield, Production of ice in tropospheric clouds: A review. *Bull. Amer. Meteor. Soc.*, 86, 795–807, 2005

Cooper, W.A. and C.P.R.Saunders, Winter storms over the San Juan Mountains. Part II: Microphysical processes, *J. Appl. Meteor.*, 19, 927–941, 1980

Cooper, W.A., and G. Vali, The origin of ice in mountain cap clouds, *J. Atmos. Sci., 38*, 1244-1259, 1981

Crosier, J., K.N. Bower, T.W. Choularton, C.D. Westbrook, P.J. Connolly, Z.Q. Cui, I.P. Crawford, G.L. Capes, H. Coe, J.R. Dorsey, P.I. Williams, A.J. Illingworth, M.W.

699 Gallagher and A.M. Blyth, Observations of ice multiplication in a weakly convective cell
700 embedded in supercooled mid-level stratus, *Atmos. Chem. Phys.*, 11, 257-273, 2011
701 Cotton, R. and P. Field, Ice nucleation characteristics of an isolated wave cloud,
702 *Q. J. Roy. Meteor. Soc.*, 128, 2417-2437, 2002
703 DeMott, P.J., A.J. Prenni, X. Liu, S.M. Kreidenweis, M.D. Petters, C.H. Twohy,
704 M.S. Richardson, T. Eidhammer and D.C. Rogers, Predicting global atmospheric ice
705 nuclei distributions and their impacts on climate, *P. Natl. Acad. Sci.*, 107, 11217-11222,
706 2010
707 DeMott, P.J., A.J. Prenni, G.R.McMeeking, R.C.Sullivan, M.D.Petters, Y.Toba,
708 M.Niemand, O.Möhler, J.R.Snider, Z.Wang and S.M. Kreidenweis, Integrating laboratory
709 and field data to quantify the immersion freezing ice nucleation activity of mineral dust
710 particles, *Atmos. Chem. Phys.*, 15, 393-409, 2015
711 Dobosy, R.J., T.L. Crawford, J.I. MacPherson, R.L. Desjardins, R.D. Kelly, S.P.
712 Oncley and D.H. Lenschow, Intercomparison among four flux aircraft at BOREAS in
713 1994, *J. Geophys. Res.-Atmos.*, 102, 29101-29111, 1997
714 Eidhammer, T., P.J. DeMott and S.M. Kreidenweis, A comparison of
715 heterogeneous ice nucleation parameterizations using a parcel model framework, *J. of*
716 *Geophys. Res.*, 114, D06202, 2009
717 Eidhammer, T., P. J. DeMott, A. J. Prenni, M. D. Petters, C. H. Twohy, D. C.
718 Rogers, J. Stith, A. Heymsfield, Z. Wang, K. A. Pratt, K. A. Prather, S. M. Murphy, J. H.
719 Seinfeld, R. Subramanian, and S. M. Kreidenweis, Ice initiation by aerosol particles:
720 Measured and predicted ice nuclei concentrations versus measured ice crystal
721 concentrations in an orographic wave cloud, *J. Atmos. Sci.*, 67, 2417-2436, 2010

722 Field, P.R., R.Wood, P.R.A.Brown, P.H.Kaye, E.Hirst, R.Greenaway and J.A.
723 Smith, Ice particle interarrival times measured with a fast FSSP, *J. Atmos. Oceanic Tech.*,
724 20, 249-261, 2003
725 Field, P.R., A.J. Heymsfield, B.J. Shipway, P.J. DeMott, K.A. Pratt, D.C. Rogers,
726 J. Stith and K.A. Prather, Ice in clouds experiment-layer clouds. Part II: Testing
727 characteristics of heterogeneous ice formation in lee wave clouds, *J. Atmos. Sci.*, 69,
728 1066-1079, 2012
729 Gardiner, B.A. and J. Hallett, Degradation of in-cloud forward scattering
730 spectrometer probe measurements in the presence of ice particles, *J. Atmos. Oceanic*
731 *Tech.*, 2, 171-180, 1985
732 Gayet, J.F., P.R.A. Brown, and F.Albers, A Comparison of In-Cloud
733 Measurements Obtained with Six PMS 2D-C Probes. J. Atmos. Oceanic Technol., 10,
734 180–194, 1993
735 Gayet, J. F., G. Febvre, and H. Larsen, The reliability of the PMS FSSP in the
736 presence of small tee crystals, *J. Atmos. Oceanic Tech.*, 13, 1300-1310, 1996
737 Hoose, C., J.E.Kristjánsson, J.-P. Chen and A. Hazra, A classical-theory-based
738 parameterization of heterogeneous ice nucleation by mineral dust, soot and biological
739 particles in a global climate model, *J.Atmos.Sci.*, 67, 2483-2503, 2010
740 Heymsfield, A.J. and D.Baumgardner, Summary of a workshop on processing of
741 2D probe data, *Bull. Amer. Meteor. Soc.*, 66, 437-440, 1985
742 Heymsfield, A.J., L.M. Miloshevich, Homogeneous ice nucleation and
743 supercooled liquid water in orographic wave clouds, *J. Atmos. Sci.*, 50, 2335–2353, 1993

744 Heymsfield, A.J., P.R.Field, M.Bailey, D.Rogers, J.Stith, C.Twohy, Z.Wang, and
745 S. Haimov, Ice in Clouds Experiment—Layer Clouds. Part I: Ice Growth Rates Derived
746 from Lenticular Wave Cloud Penetrations. *J. Atmos. Sci.*, 68, 2628–2654, 2011
747 Khain, A.P., M. Ovtchinnikov, M. Pinsky, A. Pokrovsky and H. Krugliak, Notes
748 on the state-of-the-art numerical modeling of cloud microphysics. *Atmos. Res.*, 55,159–
749 224, 2000
750 Korolev, A.V. and G.A.Isaac, Shattering during sampling by OAPs and HVPS.
751 Part I: Snow particles, *J. Atmos. Oceanic Tech.*, 22, 528-542, 2005
752 Korolev, A.V., E. F. Emery, J. W. Strapp, S. G. Cober, and G. A. Isaac,
753 Quantification of the effects of shattering on airborne ice particle measurements, *J.*
754 *Atmos. Oceanic Technol.*, 30, 2527–2553, 2013
755 Lawson, R.P., and W.A. Cooper, Performance of some airborne thermometers in
756 clouds, *J. Atmos. Oceanic Tech.*, 7, 480-494, 1990
757 Meyers, M.P., P.J. DeMott, and W.R. Cotton, New primary ice-nucleation
758 parameterizations in an explicit cloud model, *J. Appl. Meteor.*, 31, 708–721, 1992
759 Muhlbauer, A. and U.Lohmann, Sensitivity studies of aerosol–cloud interactions
760 in mixed-phase orographic precipitation, *J. Atmos. Sci.*, 66, 9, 2009
761 Murray, B.J., D. O'Sullivan, J.D.Atkinson and M.E. Webb, Ice nucleation by
762 particles immersed in supercooled cloud droplets, *Chem. Soc. Rev.*, 41, 6519-6554, 2012
763 Niemand, M., O. Möhler, B. Vogel, H. Vogel, C. Hoose, P. Connolly, H. Klein, H.
764 Bingemer, P. DeMott, J. Skrotzki and and T.Leisner, A particle-surface-area-based
765 parameterization of immersion freezing on desert dust particles, *J. Atmos. Sci., 69*, 3077–
766 3092, 2012

767 Parish, T.R., and D.Leon, Measurement of Cloud Perturbation Pressures Using an
768 Instrumented Aircraft, *J. Atmos. Oceanic Technol.*, 30, 215–229, 2013
769 Particle Measuring Systems, Passive Cavity Aerosol Spectrometer Probe
770 (Airborne), PMS Model PCASP-100X 0.10 – 3.0 µm Operating Manual, PMS Inc.,
771 Boulder, CO, 2002
772 Pokharel, B., G. Vali, Evaluation of collocated measurements of radar reflectivity
773 and particle sizes in ice clouds, *J. Appl. Meteorol.*, 50, 2104-2119, 2011
774 Pratt, K.A., P.J.DeMott, J.R.French, Z.Wang, D.L.Westphal, A.J.Heymsfield,
775 C.H.Twohy, A.J.Prenni, and K.A.Prather, In situ detection of biological particles in cloud
776 ice-crystals, *Nat. Geosci.*, 2, 398-401, 2009
777 Rodi A.R. and P.A.Spyers-Duran, Analysis of time response of airborne
778 temperature sensors, *J. Appl. Meteorol.*, 11, 554-556, 1972
779 Rogers, R.R. and M.K. Yau, *A Short Course in Cloud Physics*, 3rd ed. Permagon
780 Press, 304 pp., 1989
781 Rogers, D.C., P.J.DeMott, S.M.Kreidenweis and Y.L.Chen, A continuous-flow
782 diffusion chamber for airborne measurements of ice nuclei, *J. Atmos. Oceanic Technol.*,
783 18, 725-741, 2001
784 Richardson, M.S., P.J. DeMott, S.M. Kreidenweis, D.J. Cziczo, E.J. Dunlea, J.L.
785 Jimenez, D.S. Thomson, L.L. Ashbaugh, R.D. Borys, D.L. Westphal, G.S. Casuccio and
786 T.L. Lersch, Measurements of heterogeneous ice nuclei in the western united states in
787 springtime and their relation to aerosol characteristics, *J. Geophys. Res.*, 112, D02209,
788 2007

789 Snider, J.R., and M.D. Petters , Optical particle counter measurement of marine
790 aerosol hygroscopic growth, *Atmos. Chem. Phys.*, 8, 1949-1962, 2008
791 Strapp, J.W., W.R. Leaitch and P.S.K. Liu, Hydrated and dried aerosol-size-
792 distribution measurements from the particle measuring systems FSSP-300 probe and the
793 deiced PCASP-100x Probe, *J. Atmos. Oceanic Tech.*, *9*, 548-555, 1992
794 Strapp, J.W., F.Albers, A.Reuter, A.V.Korolev, U.Maixner, E.Rashke and
795 Z.Vukovic, Laboratory measurements of the response of a PMS OAP-2DC, *J. Atmos.*
796 *Oceanic Tech.*, 18, 1150-1170, 2001
797 Wang, Z. and K. Sassen, Cloud type and macrophysical property retrieval using
798 multiple remote sensors, *J. Appl. Meteor.*, 40, 1665–1682, 2001
799 Wang, Z., P. Wechsler, W. Kuestner, J. French, A. Rodi, B. Glover, M. Burkhart
800 and D. Lukens, Wyoming Cloud Lidar: instrument description and applications, *Opt.*
801 *Express*, 17(16), 13576-13587, 2009
802 Wang, Z., J. French, G. Vali, P. Wechsler, S. Haimov, A. Rodi, M. Deng, D. Leon,
803 J. Snider, L. Peng, Single aircraft integration of remote sensing and in situ sampling for
804 the study of cloud microphysics and dynamics, *Bull. Am. Meteorol. Soc.*, 93, 653-668,
805 2012
806 Westbrook, C.D. and A.J. Illingworth, The formation of ice in a long-lived
807 supercooled layer cloud, *Quart. J. Roy. Meteor. Soc.*, 139, 2209-2221, 2013
808 Wright, T. P., M.D.Petters, J.D.Hader, T.Morton and A.L.Holder, Minimal
809 cooling rate dependence of ice nuclei activity in the immersion mode, *J. Geophys. Res.*
810 *Atmos.*, 118, 10,535–10,543, doi:10.1002/jgrd.50810, 2013

811 Vali, G. and E.J. Stansbury, Time-dependent characteristics of the heterogeneous
812 nucleation of ice, *Can. J. Phys.*, 44, 477-502, 1966
813 Vali, G., M.K.Politovich and D.G.Baumgardner, Conduct of cloud spectra
814 measurements, Report AFGL-TR-81-0122, Air Force Geoph. Lab., Available from Nat'l.
815 Techn. Inf. Serv., Order No. AD-A102944/6, 1981
816 Vali, G. and Snider, J. R., Time-dependent freezing rate parcel model, Atmos.
817 Chem. Phys., 15, 2071-2079, 2015
818 Vali, G., Nucleation terminology, *Bull. Am. Meteorol. Soc.*, 66, 1426-1427, 1985
819 Vali, G., Interpretation of freezing nucleation experiments: Singular and
820 stochastic; sites and surfaces, *Atmos. Chem. Phys.*, 14, 5271-5294, 2014
821 Young, H.D., *Statistical Treatment of Experimental Data*, McGraw-Hill Book
822 Company, pp. 107, 1962